

UC Berkeley

UC Berkeley Previously Published Works

Title

Elucidation of Active Sites in Aldol Condensation of Acetone over Single-Facet Dominant Anatase TiO₂ (101) and (001) Catalysts

Permalink

<https://escholarship.org/uc/item/52m4h3s7>

Journal

JACS Au, 1(1)

ISSN

2691-3704

Authors

Lin, Fan
Wang, Huamin
Zhao, Yuntao
et al.

Publication Date

2021-01-25

DOI

10.1021/jacsau.0c00028

Peer reviewed

Elucidation of Active Sites in Aldol Condensation of Acetone over Single-Facet Dominant Anatase TiO₂ (101) and (001) Catalysts

Fan Lin, Huamin Wang,* Yuntao Zhao, Jia Fu, Donghai Mei,* Nicholas R. Jaegers, Feng Gao, and Yong Wang*



Cite This: *JACS Au* 2021, 1, 41–52



Read Online

ACCESS |



Metrics & More



Article Recommendations

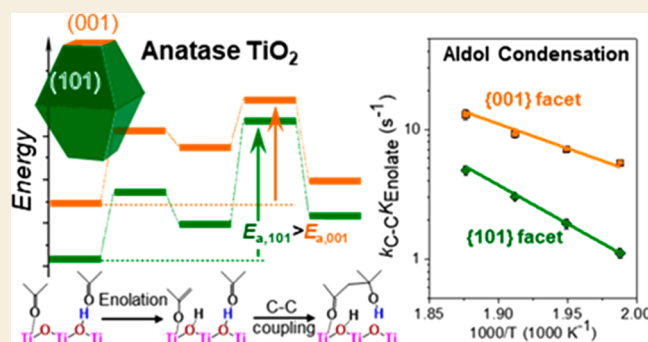


Supporting Information

ABSTRACT: Aldol condensations of carbonyl compounds for C–C bond formation are a very important class of reactions in organic synthesis and upgrading of biomass-derived feedstocks. However, the atomic level understanding of reaction mechanisms and structure–activity correlation on widely used transition metal oxide catalysts are limited due to the high degree of structural heterogeneity of catalysts such as commercial TiO₂ powders. Here, we provide a deep understanding of the reaction mechanisms, kinetics, and structure–function relationships for vapor phase acetone aldol condensation through the controlled synthesis of two catalysts with high surface areas and clean, dominant facets, coupled with detailed characterization and kinetic studies that are further assisted by density functional theory (DFT) calculations.

Temperature-dependent diffuse reflectance infrared Fourier transform spectroscopy showed the existence of abundant acetone bonded to surface hydroxyl groups (acetone–O_sH) and acetone bonded to Lewis acid sites (acetone–Ti_{5c}) on the surface of both {101} and {001} facet dominant TiO₂. Intermolecular C–C coupling of the enolate intermediate from acetone–Ti_{5c} and a vicinal acetone–O_sH is a kinetically relevant step, which is consistent with kinetic and isotopic studies as well as DFT calculations. The {001} facet showed a lower apparent activation energy (or higher activity) than the {101} facet. This is likely caused by the weaker Lewis acid and Brønsted base strengths of the {001} facet which favors the reprotonation–desorption of the coupled intermediate, making the C–C coupling step more exothermic on the {001} facet and resulting in an earlier transition state with a lower activation barrier. It is also possible that the {001} facet has a smoother surface configuration and less steric hindrance during intermolecular C–C bond formation than the {101} facet.

KEYWORDS: Single-facet catalyst, anatase titania nanocrystals, aldol condensation, kinetics, density functional theory, surface hydroxyl



INTRODUCTION

The catalytic aldol condensation of carbonyl compounds such as aldehydes and ketones forms C–C bonds and eliminates O; therefore, it has great potential for the successful upgrading of biomass-derived feedstocks, which contain smaller C chains and excess O compared to the desired fuel and chemical products.^{1–3} This reaction is a key step in many biomass conversion processes, including the Guerbet reaction of ethanol^{4–8} and saccharides to biofuel.⁹ Because of their high efficiency and low toxicity and cost, metal oxides including TiO₂,^{10–20} ZrO₂,^{18,19} CeO₂,^{13,18,21} and MgO^{12,22,23} and their combinations^{24,25} are widely used as solid acid–base catalysts in the aldol condensation reaction. Understanding the elementary steps and the active site requirements for this reaction is crucial to improving the design of the catalyst and the atomic efficiency of the oxygenate transformation processes.

TiO₂ is one of the most studied and commercialized catalytic materials.^{26,27} The mechanism of aldol condensation

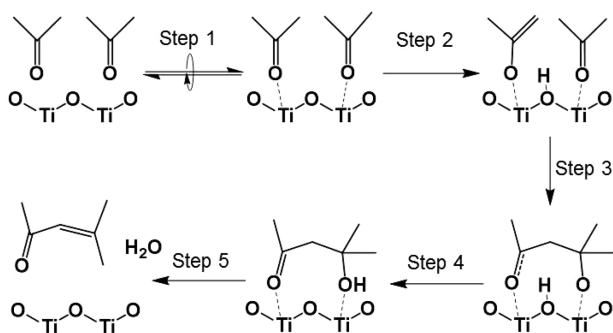
has been extensively investigated on both anatase^{10–12,14,20} and rutile TiO₂.¹⁰ It is generally accepted that aldol condensation on TiO₂ is catalyzed by Lewis acid–base site pairs (Ti–O pairs) and proceeds via enolation of the aldehyde or ketone to form an enolate intermediate, followed by C–C coupling between the enolate and an adjacent aldehyde or ketone.^{10–12,14,20,28} A more detailed proposed reaction pathway is as follows (Scheme 1): (1) first, the aldehyde or ketone molecule adsorbs on a Lewis acid site (i.e., a Ti^{δ+} cation) (Step 1); (2) the adjacent basic site (an O^{δ–} anion) then extracts the α-H of the adsorbed aldehyde or ketone to generate an enolate (Step 2); (3) the enolate C=C bond nucleophilically attacks

Received: September 21, 2020

Published: December 15, 2020



Scheme 1. Previously Proposed Elementary Steps of Acetone Aldol Condensation on an Anatase TiO₂ Surface¹⁰



the carbonyl carbon of a vicinal aldehyde or ketone molecule to create an intermolecular C—C bond (Step 3); and (4) the reprotonation of the C—C bond in the coupled intermediate generates an aldol and completes the catalytic cycle (Step 4). The unstable aldol products then dehydrate to unsaturated aldehydes or ketones (Step 5).

Although these proposed elementary steps are widely accepted, there are still debates about which step(s) are kinetically relevant. Wang et al.¹⁰ proposed that the enolate formation step, which involves the α -H extraction from the adsorbed aldehyde or ketone, is the rate-limiting step during the aldol condensation of propanal or acetone over anatase TiO₂ at low reactant surface coverages. In contrast, Zhang et al.¹¹ showed that C—C coupling between acetaldehyde and the enolate is the kinetically relevant step during acetaldehyde aldol condensation over anatase TiO₂ in the presence of cofeed ethanol. Note that in this latter case, high surface coverages of surface species (reactants, intermediates, and spectators) are registered. Young et al.¹² compared the catalytic performances of different metal oxide catalysts (anatase TiO₂, HAP (hydroxyapatite), and MgO) and proposed that reactant adsorption and product desorption are kinetically significant during acetaldehyde aldol condensation.

Aldol condensation on metal oxides is a catalytic reaction of considerable complexity. It requires both Lewis acid and Brønsted base sites and involves the participation of two adjacent reaction intermediates. Furthermore, each elementary step has different catalytic requirements (e.g., Lewis acidity, Brønsted basicity, and spatial separation of two active sites). The contradictory conclusions previously mentioned may be due to the following two causes. First, different reaction conditions were used. For example, differences in surface crowding, caused either by the selection of different reaction temperatures or by the addition of nonreactive spectators in the reaction feed, can shift rate-limiting steps from one to another. Second, mechanistic studies were carried out over the catalytic materials with complex or ill-defined structures. Fundamental investigations of aldol condensation on metal oxides are clearly disadvantageous when using commercial TiO₂ catalysts, including commercial Degussa P25,^{10,13} anatase,^{10,12} or rutile TiO₂,¹⁰ which have high degrees of surface structural heterogeneity. To circumvent these obstacles, one viable approach is to use nanosized TiO₂ model catalysts with well-controlled surface structures, specifically with preferential exposure of {101} or {001} facets. By using well-defined, single-facet dominant model catalysts, rigorous kinetic measurements on an individual facet are feasible. Such facet-dependent kinetic measurements combined with the-

oretical calculations performed on each well-defined model surface allow for (1) rigorously elucidating the reaction mechanism with kinetically relevant steps and (2) unambiguously establishing the structure–activity correlation. This approach has been recently used to elucidate the mechanism and active site requirements of alcohol dehydration on anatase TiO₂²⁹ but has not been used to study more complex aldol condensation reactions.

In this work, we synthesized two anatase TiO₂ nanocrystals, one with preferential exposure of the {101} facet and one of the {001} facet, as model catalysts. Using acetone as a model reactant and via the combination of kinetic, isotopic, infrared spectroscopic, and theoretical studies, we gain mechanistic insight into vapor phase acetone condensation on crowded TiO₂ surfaces populated with hydroxyl groups and spectator isopropanol (IPA) molecules. Such crowded hydroxylated TiO₂ surfaces are more practically relevant because (1) surface hydroxyl groups are ubiquitous on anatase TiO₂^{30,31} and (2) almost all processes involving aldol condensation (e.g., the Guerbet reaction of ethanol^{4–8}) are conducted in the presence of spectator molecules (e.g., alcohols). Unlike the aldol condensation mechanism previously proposed on clean TiO₂ surfaces without hydroxyls,^{10,17} we reveal that, on these crowded hydroxylated TiO₂ surfaces, acetone condensation between an enolate intermediate formed on the Lewis acidic Ti_{5c} site and an acetone hydrogen bonded to a vicinal surface O_sH group is the kinetically relevant step. We further showed that the {001} facet has a lower apparent activation energy for acetone aldol condensation compared to the {101} facet, consistent both density functional theory (DFT) calculations and kinetic measurement experiments. The molecular-level fundamental understanding reported here allows for the rational design of metal oxide catalysts for C—C coupling reactions.

METHODS AND MATERIALS

Catalyst Preparation and Characterization

Commercial TiO₂ (denoted as TiO₂ (P25)) was used as received (CAS#13463-67-7, Sigma-Aldrich, 21 nm in diameter, >99.5%) and was calcined at 823 K in static air for 4 h before catalytic rate measurements were taken. Facet-selective anatase TiO₂ nanocrystals ({101} facet dominant TiO₂ (101) and {001} facet dominant TiO₂ (001) samples) were synthesized with a hydrothermal method used in our previous work²⁹ (see the Supporting Information (SI) for detailed information).

The Cu/SiO₂ catalyst (~20 wt % Cu), which was used as a cocatalyst to hydrogenate the acetone condensation products and suppress the deactivation of the TiO₂ catalyst during site titration and kinetic measurement experiments, was prepared using a homogeneous deposition–precipitation method as described in the literature¹⁰ (see the SI for detailed information).

Surface area measurements were conducted on a QuantaChrome Autosorb-6 using N₂ adsorption isotherms and BET (Brunauer–Emmett–Teller) surface area analysis methods. Samples were degassed under vacuum at 423 K for 4 h before adsorption measurements.

Scanning electron micrographs were acquired using a FEI Helios 600 NanoLab FIB-SEM instrument. Transmission electron microscopy (TEM) was performed using a JEOL JEM 2010 instrument operating at 200 keV. The TEM specimens were prepared by dispersing calcined TiO₂ samples in ethanol and depositing the suspension onto a lacey carbon-coated copper grid.

Catalytic Rate Measurements

The rates of acetone aldol condensation were measured in a fixed-bed quartz reactor (inner diameter of 10 mm) with plug-flow fluid dynamics. Either the TiO₂ catalysts or the TiO₂ + Cu/SiO₂ physical mixtures (obtained by crushing and mixing the two catalysts with a mortar and pestle) were pressed, crushed, and sieved to retain particles of 180–250 μm across for the rate measurement. For the mixtures, the TiO₂-to-Cu/SiO₂ ratios for TiO₂(101) and TiO₂(001) were 1:2 and 5:2, respectively, because of their ~5× difference in surface area. The catalysts (10–25 mg) were mixed with 200 mg of SiC (200 mesh, Sigma-Aldrich) and loaded into the reactor. The reactor was contained within a resistively heated furnace with its temperature controlled by a digital feedback controller (Omega, CN3251). Inside the quartz reactor, the catalysts were supported on a coarse quartz frit and the bed temperature was recorded using a K-type thermocouple placed at the center of the catalyst bed. The catalysts were pretreated by being heated to 823 K in flowing air (40 cm³ min⁻¹, Zero grade, Oxarc) at 10 K min⁻¹ and holding for 1 h, followed by purging in He (for TiO₂, 100 cm³ min⁻¹, Ultra High Purity grade, Oxarc) or reducing in a 10% H₂/He mixture (for the TiO₂-Cu/SiO₂ mixture, 100 cm³ min⁻¹, Ultra High Purity grade, Oxarc) at rate measurement temperatures (483–523 K) for 30 min.

The reactants, acetone (Sigma-Aldrich, >99.9%), acetone-*d*₆ (Sigma-Aldrich, >99.9%), and IPA (Sigma-Aldrich, >99.9%), were introduced into a vaporization zone located upstream of the reactor through gastight syringes (Hamilton, model 1002, 2.5 mL, or model 1005, 5 mL), mounted on syringe infusion pumps (KD Scientific, LEGATO 100 and model 100). The vaporization zone was heated to 348 K, allowing the reactants to evaporate and mix with a flowing He or H₂/He stream (Ultra High Purity grade, Oxarc). The respective partial pressures of the reactants were adjusted by controlling the liquid injection rates of the syringe infusion pumps. The mixture was fed to the reactor via heated transfer lines whose temperature was held at 473 K. The effluent stream was kept above 473 K and quantified with an online gas chromatograph (Agilent, 7890A) equipped with a capillary column (Agilent HP-1 (19091Z-433, 30 m, 0.25 mm ID, 0.25 μm film) connected to a flame ionization detector.

Our previous work has confirmed that these TiO₂ catalysts do not contain active Brønsted acid sites.²⁹ However, we found that the Cu/SiO₂ cocatalyst did contain a small number of Brønsted acid sites catalyzing acetone condensation reactions. Thus, 2,6-ditertbutylpyridine (DTBP) was cofeed (acetone/DTBP = 500:1) to selectively poison the Brønsted acid sites during rate measurements.

Before the rate measurement, the reactant mixture stream flow through a gas line and bypassed the reactor, a process that was monitored by using a gas chromatograph (GC). When the reactant partial pressures stabilized, the stream was switched to the reactor, and the reactor effluent was sampled and analyzed by the GC every 20 min. The partial pressures of the reactants were adjusted during the GC sampling intervals. The rates at a specific set of conditions (reactant partial pressures) were measured multiple times throughout the course of an experiment. These rates could also be used with nonlinear interpolation to estimate the number of active sites present at any given time during the experiment:

$$r_{gt} = \text{TOF} \times [L]_t = r_{g0} \exp(-k_d t) = \text{TOF} \times [L]_0 \exp(-k_d t) \quad (1)$$

where *t* represents the time-on-stream; *r*_{gt} and *r*_{g0} are the rates of acetone condensation depending on the weight of the catalyst at the times *t* and 0, respectively; TOF is the turnover frequency; and [L]_{*t*} and [L]₀ are the Lewis acid site densities at times *t* and 0, respectively. *k*_d is the deactivation rate constant at a given condition (temperature and reactant partial pressures).

The initial densities of the Lewis acid-Brønsted base site pairs (Ti–O pairs) on the catalysts [L]₀ were measured using in situ titration with propionic acid (Sigma-Aldrich, >99.5%) during acetone aldol condensation reaction at 453 K. This titration method was adopted from recent literature by Wang et al.¹⁰ Here, 100–150 mg of TiO₂(101)–Cu/SiO₂ or TiO₂(001)–Cu/SiO₂ particles was mixed

with 600 mg of SiC, loaded into the reactor, and heated to the desired titration temperature (453 K) in flowing H₂/He (20 kPa H₂). Acetone (0.65 kPa) was introduced onto the catalyst first (in 20 kPa H₂). After the acetone condensation rates reached a steady state, the reactant feed was switched to a mixture of acetone and propionic acid (molar ratio of 180:1). The concentrations of the reactant (acetone), titrant (propionic acid), and products in the effluent were measured by using the GC as described above. The number of Ti–O site pairs accessible to the examined TiO₂ catalysts was determined from the amount of propionic acid required to fully suppress condensation rates using propionic acid/(Ti–O) stoichiometry of 1.¹⁰

Infrared Spectroscopic Studies

Diffuse reflectance infrared Fourier transform spectroscopy (DRIFTS) studies of the adsorption and temperature-programmed desorption (TPD) of acetone on TiO₂(101) and TiO₂(001) catalysts were performed on a Nicolet iS50R FT-IR spectrometer (Thermo Scientific) equipped with a liquid-nitrogen-cooled MCT detector and a Praying Mantis diffuse reflection accessory (Harrick Scientific Products Inc.) operated at a resolution of 4 cm⁻¹. The catalyst powders placed in the sample cell were pretreated by heating to 673 K and holding for 30 min, followed by cooling down to 293 K in flowing He (20 mL min⁻¹). The background spectra were collected under flowing He (10 mL min⁻¹) at measurement temperatures of 293, 323, 373, 423, 473, 523, and 573 K and were used as backgrounds for the spectra collected at the same temperatures. For acetone adsorption at 293 K, the acetone was dosed into the sample cell by flowing the carrier gas (He, 10 mL min⁻¹) through a bubbler containing acetone (placed in an ice bath) for 10 s for each dose before transitioning to pure He for purging. After the TiO₂ surface was saturated with acetone after four or five doses, the sample was purged by flowing He (10 mL min⁻¹) through it for 30 min to remove both physisorbed and gaseous acetone in the cell. TPD was performed by heating the sample at a rate of 10 K min⁻¹ and holding at each measurement temperature for 1 min to collect spectra.

Density Functional Theory Calculations

All spin-polarized DFT calculations were carried out using the gradient-corrected Perdew, Burke, and Ernzerhof functional³² implemented in the CP2K package.³³ The effective cores were described by the Goedecker–Teter–Hutter pseudopotentials.^{34–36} The valence electrons of all atoms were expanded in the double- ζ Gaussian basis sets, with an energy cutoff of 500 Ry. Only the γ -point was used to sample the Brillouin zone, and the van der Waals correction proposed by Grimme et al.³⁷ was included in all calculations. As indicated in the previous studies, DFT+U method should be applied.^{38–41} In the work, an effective U–J value of 4.70 eV was used in all calculations. The transition states of all elementary steps were searched with the climbing-image nudged elastic band method until the maximum force was converged to less than 0.05 eV/Å. The transition structure for each elementary step in the aldol condensation reaction was further confirmed by identifying the only single imaginary frequency along the reaction coordinate. The zero point energy (ZPE) correction was taken into account in the calculation.

In the present work, the periodic TiO₂ {101} and {001} surfaces consist of four and six TiO₂ unit layers, respectively, and were constructed from the anatase TiO₂ bulk. Each TiO₂{101} layer consists of 12 Ti atoms, six of which are active five-coordinated (Ti_{5c}), and 24 O atoms, six of which are exposed two-coordinated (O_{2c}). For the TiO₂{001} surface, nine equivalent five-coordinated Ti_{5c} and 18 O atoms, nine of which are two-coordinated O_{2c}, are in each TiO₂ layer. It is expected that the five-coordinated Ti_{5c} and two-coordinated O_{2c} atoms serve as the active Lewis acid and Brønsted base sites, respectively. To eliminate the unphysical interactions of the periodic {101} and {001} surface slabs, a vacuum space of 15 Å in the *z* direction was used for both the TiO₂ {101} and {001} surface model systems. To mimic the practical hydroxylated TiO₂ {101} and {001} model surfaces as suggested in our experiments, two hydroxylated TiO₂ {101} and {001} model surfaces were used in the calculations. Upon the optimization of two surface slabs, the atoms in the bottom

two layers of the $\text{TiO}_2(001)$ surface are fixed while all atoms in the $\text{TiO}_2(101)$ surface are relaxed in the calculations of aldol condensation reaction.

RESULTS AND DISCUSSION

Structural and Physicochemical Properties of Anatase $\text{TiO}_2(101)$ and $\text{TiO}_2(001)$ Model Catalysts

Figure 1 shows the TEM images of the $\text{TiO}_2(101)$ and $\text{TiO}_2(001)$ nanocrystals, and Table 1 lists their physicochem-

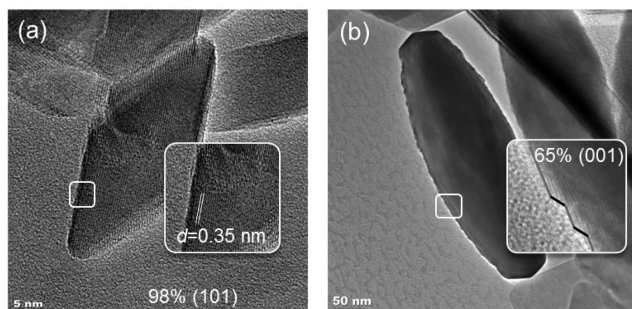


Figure 1. TEM images of (a) $\text{TiO}_2(101)$ and (b) $\text{TiO}_2(001)$ nanocrystals.

Table 1. Physicochemical Properties of the $\text{TiO}_2(101)$ and $\text{TiO}_2(001)$ Model Catalysts

	$\text{TiO}_2(101)$	$\text{TiO}_2(001)$
surface area ($\text{m}^2 \text{g}^{-1}$) ^a	45.2	8.4
{101} facet fraction ^b	98%	35%
{001} facet fraction ^b	2%	65%
Lewis acid–base site pair density (nm^{-2}) ^c	0.92	0.95
Lewis acid–base site pair density on facet (nm^{-2})	0.92{101}	0.97{001}

^aSurface area was measured by N_2 adsorption isotherms and BET analysis methods. ^bThe fractions of the {101} and {001} facets were determined through analysis of TEM images of catalyst nanocrystals. ^cThe density of the Lewis acid–base site pairs was determined by in situ titration with propionic acid during an acetone aldol condensation reaction at 453 K (see section S3 in the SI).

ical properties. The $\text{TiO}_2(101)$ sample has smaller particle sizes than those in the $\text{TiO}_2(001)$ sample, as shown in Figure 1, resulting in the former having a higher surface area (Table 1). The {101} particles are bipyramidally shaped, where the dominant exposed facets are {101}, as indicated by the interplanar spacing of 0.35 nm (Figure 1a) parallel to the exposed surfaces. Both ends of the bipyramids are {001} facets. By carefully examining a large number of particles, it was estimated that approximately 98% of the exposed surface in this sample has the {101} facet. In contrast, particles in the $\text{TiO}_2(001)$ sample are plate shaped with uneven thicknesses (shorter at the ends). Examinations of the extended plate surfaces reveal that the exposed surfaces have alternative {001} and {101} facets, as indicated by the inset in Figure 1 ({001} in red and {101} in black). The edges of the platelike crystals are the {101} facets. Again, by examining multiple crystals, it is estimated that approximately 65% of the surface on $\text{TiO}_2(001)$ has the {001} facet (Figure 1b). The remaining facets are largely {101}. For the kinetic measurements, the catalytic activity for the {101} facet was directly measured using a $\text{TiO}_2(101)$ sample; activity for the {001} facet was determined

after subtracting the activity contribution of the 35% {101} facet from the $\text{TiO}_2(001)$ sample.

Kinetic Study of Aldol Condensation on Anatase TiO_2 Catalysts

Accurate kinetic measurements of acetone aldol condensation on heterogeneous catalysts are often impeded by their rapid deactivation due to coke formation. Figure 2 shows the

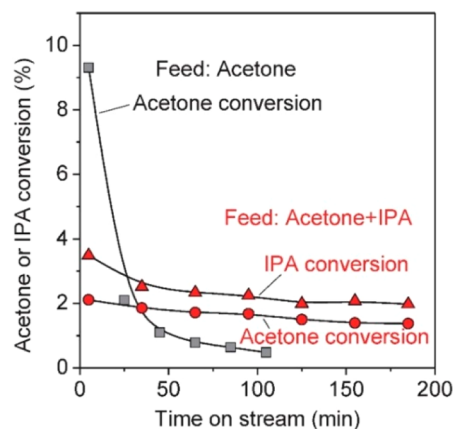


Figure 2. Conversions of acetone or IPA on $\text{TiO}_2(\text{P}25)$ at 523 K as a function of time-on-stream upon feeding acetone (0.55 kPa) alone (space velocity = $0.035 \text{ mmol}_{\text{acetone}}(\text{g}_{\text{cat}} \cdot \text{s})^{-1}$) or cofeeding acetone (0.47 kPa) + IPA (0.65 kPa) (space velocity = $0.03 \text{ mmol}_{\text{acetone}}(\text{g}_{\text{cat}} \cdot \text{s})^{-1}$).

conversion of vapor phase acetone condensation reactions on $\text{TiO}_2(\text{P}25)$ at 523 K as a function of time-on-stream. When feeding acetone is the only reactant, the acetone conversion drops rapidly within the initial 40 min by 1 order of magnitude. Such dramatic catalyst deactivation during an acetone reaction makes it difficult to reach a steady state and therefore to carry out accurate site titration and rate measurements as required for turnover rate determination. This impediment occurs because the primary acetone aldol condensation forms C_6 alkenone (mesityl oxide) and the sequential secondary or even tertiary condensation reactions further lead to the formation of heavy products (e.g., C_9 and C_{12} oxygenates, hydrocarbons, and cokes) that deposit on the catalysts and block the active sites.^{11,12,15}

To mitigate the deactivation of catalysts, the rates of acetone aldol condensation on TiO_2 catalysts were measured in the presence of IPA in this work. As shown in Figure 2, when cofeeding acetone and IPA together on $\text{TiO}_2(\text{P}25)$ at 523 K, both acetone aldol condensation and IPA dehydration occurred simultaneously. The conversions of both acetone and IPA remained stable within 3 h of reactions. The presence of IPA effectively mitigates the catalyst deactivation because IPA dilutes the surface acetone coverages, which reduces the formation of heavy products from consecutive condensation reactions. Such a slow deactivation allows measured rates to be corrected by recording rates under a given set of conditions multiple times throughout the course of an experiment and by using linear interpolation to estimate the number of active sites present at any given time during the experiment. Next, the reaction kinetics of acetone aldol condensation in the presence of an IPA spectator will be discussed in greater detail.

As discussed in the Introduction (Scheme 1), aldol condensation on TiO_2 proceeds via an enolation step that converts a ketone or aldehyde into an enolate intermediate

(Step 2); this is followed by a C–C coupling step that occurs between the enolate intermediate and another ketone or aldehyde (Step 3). The subsequent dehydration of the unstable aldol products (Step 5) is rapid and kinetically irrelevant because the aldols (e.g., diacetone alcohol) cannot be detected at the temperatures studied (>473 K). There are debates on whether the enolation or the C–C coupling is the rate-limiting step.

Here, to verify whether enolate formation is the rate-limiting step, we examined the kinetic isotope effects (KIEs) of deuterium-labeled acetone (C_3D_6O , acetone- d_6). As shown in Figure 3, on both $TiO_2(101)$ and $TiO_2(001)$, acetone

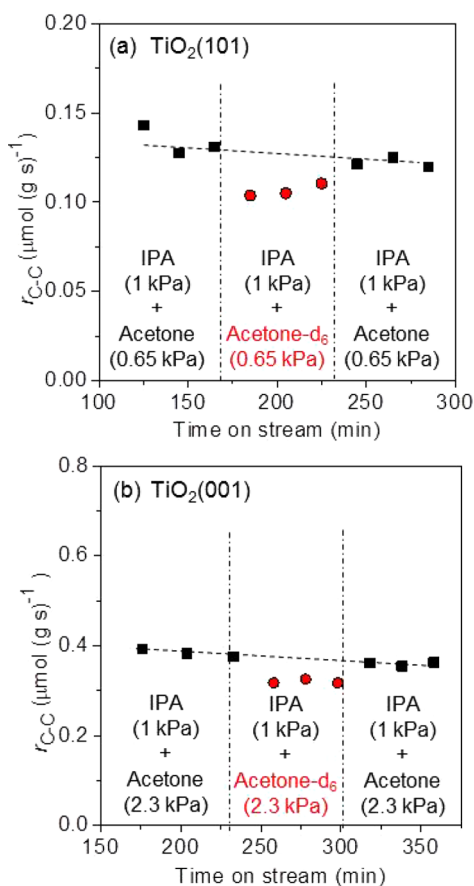


Figure 3. Rates of acetone (or acetone- d_6) aldol condensation as a function of time-on-stream on (a) $TiO_2(101)$ and (b) $TiO_2(001)$ at 503 K (IPA = 1 kPa and acetone (or acetone- d_6) = 0.65 kPa for $TiO_2(101)$ and 2.3 kPa for $TiO_2(001)$).

condensation rates of acetone- d_6 , $r_{C-C,D}$, are only slightly lower than those of normal acetone- h_6 , $r_{C-C,H}$ ($r_{C-C,H}/r_{C-C,D}$ ratio = 1.18 ± 0.08 and 1.16 ± 0.08 , respectively), under constant partial pressures of acetone- h_6 /acetone- d_6 (0.65 or 2.3 kPa) and IPA (1 kPa). Such a weak KIE suggests the kinetic irrelevance of the enolate formation (Step 2, Scheme 1), which involves the C–H (or C–D) cleavage on the α -carbon. Similar conclusions have previously been drawn via KIE assessment of aldol condensation in either the presence or absence of alcohol.^{11,12} Zhang et al.¹¹ reported a much lower KIE ($r_{C-C,H}/r_{C-C,D}$ ratio = 0.6) for an acetaldehyde–ethanol mixture on TiO_2 ; whereas Young et al.¹² observed no KIE for acetaldehyde aldol condensation on TiO_2 , MgO, and HAP catalysts, in the absence of alcohol. In contrast, Wang et al.¹⁰

reported a much higher KIE ($r_{C-C,H}/r_{C-C,D}$ ratio = 2.4) for reactions in the reactant stream of acetone–IPA– H_2 (D_2) on a TiO_2 –Cu/ SiO_2 catalyst mixture, suggesting the kinetic relevance of enolation step. Zhang et al.¹¹ attributed the disagreement among different studies to a change of acetone coverage which potentially could lead to the transition of kinetically relevant step (e.g., from C–C coupling step to enolation step).

Here in, we then assessed the KIEs of acetone condensation in the regime of higher acetone coverage. By using reactant mixtures with a much lower IPA ratio (IPA = 0.09 kPa, acetone = 1.2 or 2.2 kPa) to increase acetone coverage, we still observed similar weak KIEs (1.05 ± 0.07 and 1.09 ± 0.08 for acetone pressures of 1.2 and 2.2 kPa, respectively, Figure S5a). We further examined the KIE in the absence of IPA (Figure S5b). Without IPA addition, the TiO_2 catalysts deactivated rapidly with time-on-stream during the reaction reactions. Nevertheless, upon extrapolating to a time-on-stream of 0, almost identical initial rates of aldol condensation were found for acetone- h_6 and acetone- d_6 ($r_{C-C,H}/r_{C-C,D}$ ratio = 1.04 ± 0.09). These results indicate that, regardless of acetone coverage studied in this work, enolate formation (α -C–H cleavage) always remains kinetically irrelevant.

Because enolate formation (Step 2, Scheme 1) is not the rate-limiting step, the C–C coupling step is likely kinetically relevant and determines acetone aldol condensation rate (Step 3, Scheme 1), as proposed by Zhang et al.¹¹ We further confirmed this by the power-law dependence measurements shown below. Figure 4 shows acetone aldol condensation rates on $TiO_2(101)$ and $TiO_2(001)$ at 523 K as a function of acetone pressure (P_{one}) under different constant IPA pressures (P_{IPA}). At a constant IPA pressure, the rates of acetone aldol condensation are nearly second-order on the acetone partial pressures ($r_{C-C} \propto P_{\text{one}}^{1.8-1.9}$). On the other hand, under a constant acetone pressure, the aldol condensation shows a negative reaction order over IPA pressure ($r_{C-C} \propto P_{\text{IPA}}^{-1.3 \sim -1.6}$ for $TiO_2(101)$ and $r_{C-C} \propto P_{\text{IPA}}^{-1.2 \sim -1.5}$ for $TiO_2(001)$). The reaction order for IPA is lower than -1 , which indicates that the C–C coupling step likely proceeds via a Langmuir–Hinshelwood mechanism. This mechanism requires the participation of two acetone molecules adsorbed on vicinal active sites. In the next section, the site requirements for acetone condensation on a TiO_2 surface are discussed in greater detail.

It is also noted that, under identical conditions (same P_{IPA} , P_{one} , and temperature), $TiO_2(101)$ has a higher r_{C-C} than $TiO_2(001)$. This r_{C-C} comparison, however, does not necessarily reflect the trend of the intrinsic activities of acetone condensation on these two catalysts. Our previous work²⁹ showed that IPA adsorbs much stronger on $\{001\}$ than on $\{101\}$ facets; therefore, acetone adsorption on these two facets encounters different extents of adsorption completion by the IPA spectator. In the following sections, we will measure the intrinsic rate constants for acetone condensation on these two facets to compare their activities.

Site Requirements for Acetone Condensation on a TiO_2 Surface

As proposed in previous literature, ketone or aldehyde aldol condensation on anatase TiO_2 occurs between two ketone or aldehyde molecules adsorbed on two vicinal Ti sites of TiO_2 ,¹⁰ as depicted in Scheme 1. Regarding this mechanism, we conducted theoretical modeling on the anatase $\{101\}$ facet (Figure S6 in the SI), which shows that the transition state for

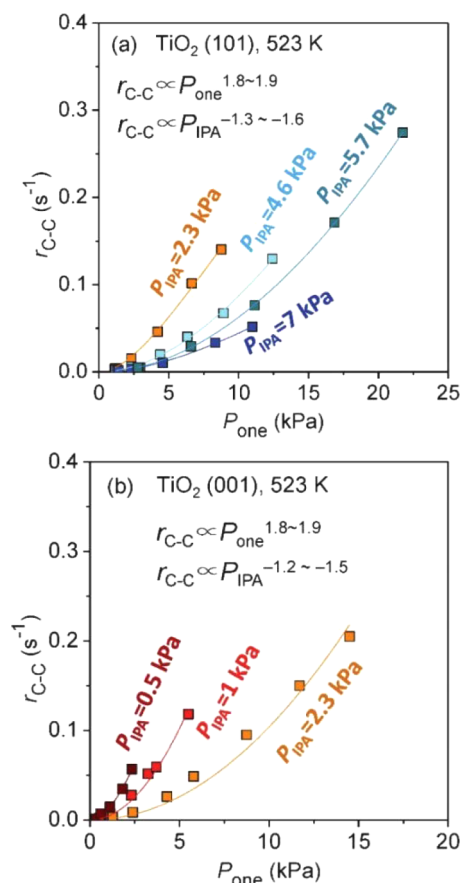


Figure 4. Rates (normalized to total number of Lewis acid site pairs) of acetone condensation (r_{C-C}) on (a) $\text{TiO}_2(101)$ and (b) $\text{TiO}_2(001)$ at 523 K as a function of acetone pressure (P_{one}) under constant IPA pressure (P_{IPA}).

the α -H extraction has the highest energy along the reaction coordinate, making enolation the rate-limiting step. This is consistent with the DFT results reported by Wang et al.¹⁰ However, our kinetic measurements (as discussed in the previous section) indicate that the C–C coupling was the kinetically relevant step for acetone condensation under our reaction conditions (i.e., in the presence of a coadsorbed spectator IPA molecule). Such an inconsistency between previously reported theory work and our experimental results in terms of kinetically relevant steps may suggest that different mechanisms were involved as a result of the different experimental conditions. Next, we combined infrared spectroscopic study and theoretical modeling to elucidate the site requirements for acetone condensation under the conditions relevant to our studies.

We first examined acetone adsorption on an anatase TiO_2 surface by DRIFTS. Figure 5a and b show the infrared spectra for the adsorption and temperature-programmed desorption of acetone (acetone TPD) on $\text{TiO}_2(101)$ and $\text{TiO}_2(001)$ catalysts, respectively. Upon acetone adsorption at room temperature, the stretching vibration of adsorbed carbonyl groups ($\nu(\text{C}=\text{O})$) was observed at around 1700 cm^{-1} . Interestingly, two overlapping peaks at 1707 and 1694 cm^{-1} , respectively, developed simultaneously, indicating the presence of two different types of adsorbed acetone molecules. As informed by the literature, the band at 1694 cm^{-1} is ascribed to acetone adsorbed on the Lewis acid site (Ti)^{16,42–45} and the

band at 1707 cm^{-1} is related to either acetone bonded to a weaker Lewis acid site or nonacidic site (e.g., a nonacidic hydroxyl group^{44–46}) or multilayer adsorbed acetone.⁴² The peak deconvolution of the $\nu(\text{C}=\text{O})$ bands (as shown in the inserts in Figure 5a and b) indicates that the amounts of these two types of adsorbed acetone are comparable. The participation of surface hydroxyl groups (O_sH) in acetone adsorption was confirmed by the appearance of three negative peaks at the vibration region of TiO_2 surface O_sH groups upon acetone adsorption. These O_sH vibrations were attributed to terminal hydroxyl groups (Ti–OH) at 3740 cm^{-1} and two types of bridging hydroxyl groups (Ti–OH–Ti) at 3674 and 3694 cm^{-1} , respectively. The interactions between O_sH groups and adsorbed acetone molecules shift the vibration of O_sH groups ($\nu(\text{O}–\text{H})$) to lower frequencies, which is shown as a broad positive band at 3540 cm^{-1} . This 3540 cm^{-1} band is not likely the gaseous acetone C=O stretching overtone, which is typically narrower and locates at lower frequencies (3450 – 3470 cm^{-1}).⁴⁷ As the temperature increased, these O_sH groups were recovered because of desorption or condensation reactions of surface acetone molecules. As shown in Figure 5c, for both $\text{TiO}_2(101)$ and $\text{TiO}_2(001)$ samples, the $\nu(\text{C}=\text{O})$ band at 1707 cm^{-1} was proportional to the total negative peaks of O_sH groups during the entire adsorption and desorption experiment. This unambiguously suggests that the 1707 cm^{-1} band belongs to the acetones hydrogen-bonded to the surface OH groups. These assignments for the observed IR spectra were further confirmed by our DFT calculations (Table S1).

Figure 5d shows the total intensity of the $\nu(\text{C}=\text{O})$ bands at different temperatures ($I_{\nu(\text{C}=\text{O}),T}$) relative to those at 298 K ($I_{\nu(\text{C}=\text{O}),298\text{K}}$), which reflects the acetone coverage as a function of temperature. As the temperature increased, the $\nu(\text{C}=\text{O})$ bands decreased faster on $\text{TiO}_2(001)$ than on $\text{TiO}_2(101)$. This suggests either weaker acetone adsorption, faster acetone condensation on $\text{TiO}_2(001)$, or both.

Because of the abundance of acetones hydrogen bonded to the surface O_sH groups as confirmed by DRIFTS, we propose here that, besides the condensation pathways depicted in Scheme 1, the intermolecular C–C coupling can also occur between an enolate intermediate formed on a Ti site and an acetone hydrogen bonded to a vicinal surface O_sH group. A similar mechanism has previously been proposed for the self-condensation of *n*-valeraldehyde on TiO_2 .¹⁶ As depicted in Scheme 2, acetone molecules first adsorb on both the Ti site and the vicinal O_sH group, reaching equilibrium (Steps I and II, Scheme 2). The basic O site of the Ti–O pair could extract the α -H of the Ti-bonded acetone, forming an enolate intermediate (Step III, Scheme 2). Sequentially, the enolate C=C bond nucleophilically attacks the carbonyl carbon of the O_sH -bonded acetone, leading to the aldol product via an intermolecular C–C bond formation (Step IV, Scheme 2). The validity of this mechanism was examined using the DFT calculations described below.

Aldol condensation between two acetone molecules adsorbed on a Ti_{sc} site and a vicinal $\text{O}_{\text{c}}\text{H}$ group on hydroxylated $\text{TiO}_2\{101\}$ and $\{001\}$ surfaces was studied using DFT calculations. For the high energy anatase $\{001\}$ facet, the (1×4) reconstruction, which can totally change the catalytic activity of the surface, has always been a concern. However, to the best of our knowledge, the (1×4) reconstruction has only been observed under strictly controlled conditions, including high temperature (773 – 1073 K),^{48–53} ultrahigh vacuum^{48–50} or low pressure (e.g., 10^{-3} – 10^{-2} Pa

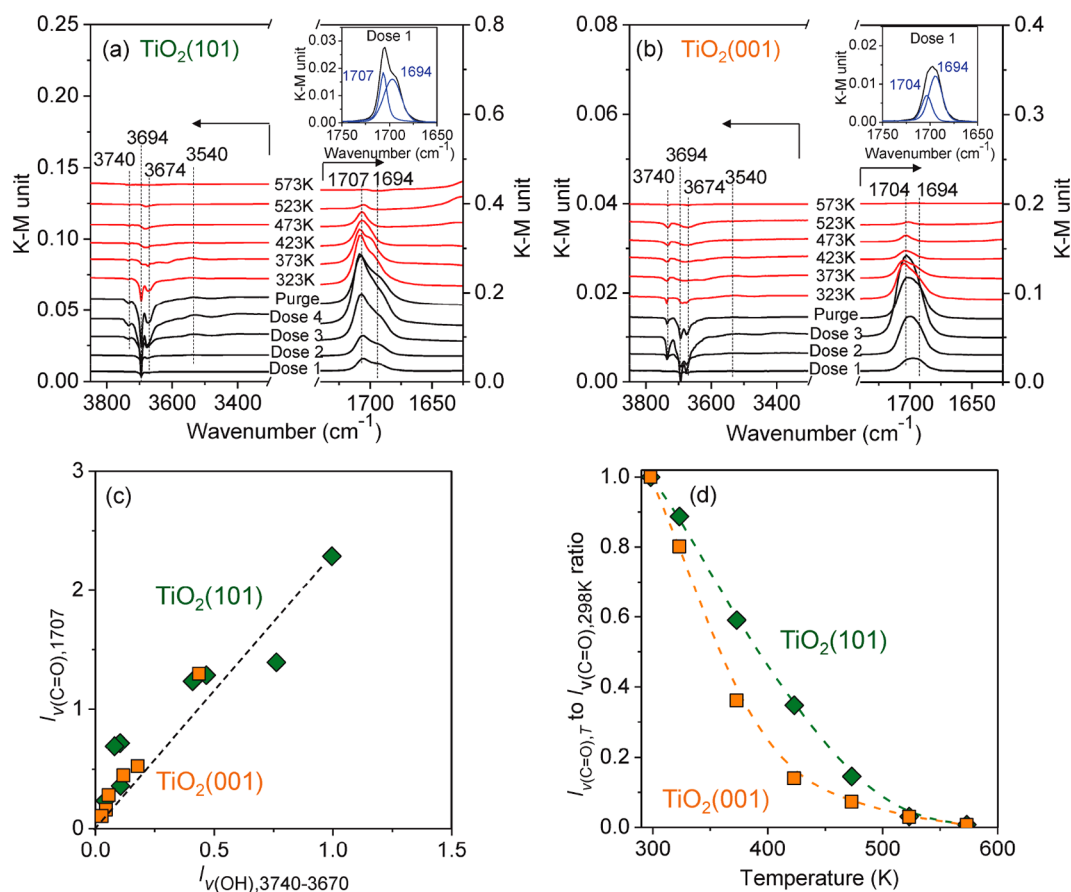
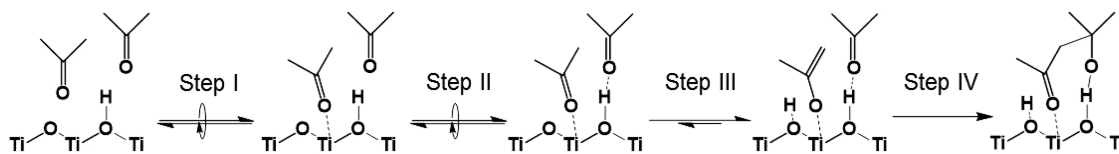


Figure 5. (a, b) DRIFTS spectra for acetone adsorption (black lines, 303 K, acetone vapor dose in He) and temperature-programmed desorption (red lines, desorption in flowing He) on (a) TiO₂(101) and (b) TiO₂(001) catalysts (inserted figures show the examples of peak deconvolution for the $\nu(\text{C}=\text{O})$ band). (c) Intensity of the band at 1707 cm⁻¹ ($I_{\nu(\text{C}=\text{O}),1707}$) as a function of the intensity of the negative OH bands ($I_{\nu(\text{OH}),3740-3670}$). (d) Intensity of the $\nu(\text{C}=\text{O})$ bands at different temperatures ($I_{\nu(\text{C}=\text{O}),T}$) relative to that at 298 K ($I_{\nu(\text{C}=\text{O}),298\text{K}}$) as a function of temperature.

Scheme 2. Proposed Elementary Steps of Acetone Aldol Condensation on a TiO₂ Surface, With C–C Coupling Occurring between the Enolate Formed on the Ti Site and the Acetone Hydrogen Bonded to the Surface Hydroxyl Group



O₂)^{48,51,52} environment, and bare {001} surfaces cleaned with ion sputtering^{48,50} or electron-beam irradiation.⁵² In this work, the TiO₂(001) sample was simply calcined at 823 K in air. In addition, the OH groups can stabilize the surface structure, making the (1 × 4) reconstruction unlikely to happen. The calculated energy profiles of the enolization and C–C coupling steps (Steps III and IV, Scheme 2) are shown in Figure 6, where the zero energy corresponds to two acetone molecules in the gas phase away from TiO₂ surface. More detailed structures are provided in Figure S8, and overall energy diagrams from the initial reactant state to the product state are provided in Figure S9. Two acetone molecules generally adsorb stronger on the {101} facet than on the {001} facet, as indicated by the more negative energies of acetone adsorption at both the Ti_{5c} site (−103 vs −70 kJ mol⁻¹) and the O_sH group (−87 vs −55 kJ mol⁻¹). This suggests a stronger Lewis acid strength of the {101} facet than that of the {001} facet which is consistent with the trend determined by pyridine-TPD in our previous work.²⁹

For the enolization step (Step III), the abstraction of α -H was achieved on a surface two-coordinated O_{2c} site vicinal to the Ti_{5c} with adsorbed acetone. The reaction barriers and energies for the α -H abstraction step were calculated to be 67 kJ mol⁻¹ and 45 kJ mol⁻¹ on the TiO₂ {101} surface and 76 kJ mol⁻¹ and 71 kJ mol⁻¹ on the TiO₂ {001} surface. This suggests that enolate formation is more favorable on {101} than {001} surfaces because the stronger Lewis acid (Ti_{5c}) and base (O_{2c}) strengths of the {101} surface favor the polarization of Ti_{5c}-bonded acetone and the abstraction of α -H as a proton.

After the α -H activation, the enolate nucleophilically attacks the carbon center of the carbonyl bond in acetone that is hydrogen-bonded to a vicinal O_sH group, producing the aldol product (Step IV). The C–C coupling barriers on the TiO₂ {101} and {001} facets are 120 kJ mol⁻¹ (from −145 to −25 kJ mol⁻¹) and 50 kJ mol⁻¹ (from −54 to −4 kJ mol⁻¹), respectively. These calculation results show that the potential energy of the C–C coupling transition state (TS_{C–C}) is higher than that of the α -H abstraction transition state (TS_{Enolate}),

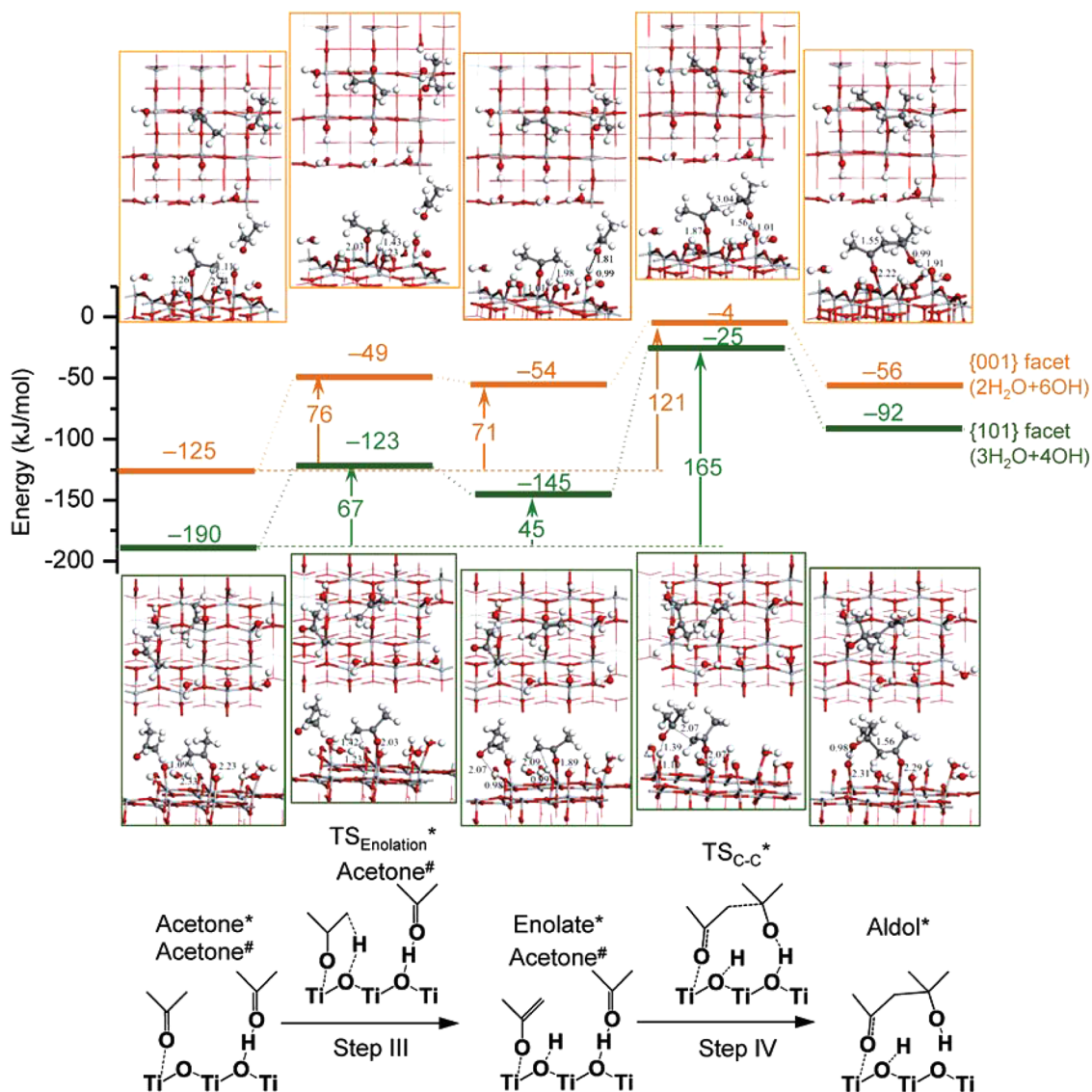


Figure 6. Potential energy profiles and intermediate structures of acetone condensation on {001} (orange) and {101} (green) facets of anatase TiO_2 , with the zero energy corresponding to two acetone molecules in the gas phase away from TiO_2 surface (* and # represent the Ti site and surface OH group, respectively).

making the C–C coupling step kinetically relevant and determining the rate on both the TiO_2 {101} and {001} facets. This is consistent with observations from the kinetic measurements (Figure 4) and the isotopic experiments (Figure 3). In this reaction model, the TiO_2 {001} facet has a much lower apparent activation energy for acetone aldol condensation than the {101} facet (121 vs 165 kJ mol^{-1}). This trend of activity on these two facets was further confirmed by kinetic measurements, as discussed in the following section.

Although we could not rule out the occurrence of C–C coupling between two adjacent Ti_{5c} -bonded acetone molecules (as shown in Scheme 1), it is likely that the interaction between the Ti_{5c} -bonded and O_sH -bonded acetones becomes the predominant route on the TiO_2 surface populated with O_sH groups and IPA spectators. On the TiO_2 surface, interactions between two Ti_{5c} -bonded acetone molecules is largely impeded by the IPA spectators, the O_sH -bonded acetone molecules, or both. We also simulated the reaction between two Ti_{5c} -bonded acetones on O_sH populated TiO_2 {101} surface, which showed that one of the Ti_{5c} -bonded

acetone will end up with bonding to O_sH when attacking the enolate (Figure S10) for C–C coupling step and again C–C coupling is the rate-limiting step. A similar transition of the kinetically relevant step due to the change in surface crowdedness was observed by Ngo et al. during aldol condensation of cyclopentanone over hydrophobized MgO catalysts in the liquid phase.⁵⁴ On the pristine hydrophilic MgO catalyst, where acid–base pairs are fully available on the surface, the rate-limiting step for cyclopentanone aldol condensation is the enolate formation via α -H abstraction at a basic site. In contrast, on the MgO catalyst hydrophobized by octadecyltrichlorosilane (OTS), where the grafted OTS molecules interfere between active sites and impede the adsorbate–adsorbate interactions, the bimolecular C–C coupling becomes the rate-limiting step. On this OTS-crowded surface, H_2O molecules can bridge the polarizing effect of a remote Lewis acidic Mg site to the carbonyl O of the cyclopentanone hydrogen bonded to the H_2O bridge; this initiates C–C coupling between a Mg-bonded cyclopentanone and a hydrogen-bonded cyclopentanone.

Kinetic Consequences of the Facet Configuration during Acetone Condensation

To probe the kinetic consequences of the facet configuration on acetone condensation, we carried out rate measurements to attain rate constants for the kinetically relevant C–C coupling step on TiO₂(101) and TiO₂(001) samples. The rate for the {101} facet was directly derived using the rate of the TiO₂(101) sample; the rate for the {001} facet was determined after subtracting the contribution of the 35% {101} facet from the TiO₂(001) sample.

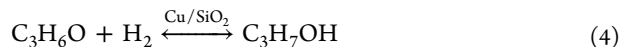
Equation 2 is the rate expression for acetone condensation (r_{C-C} , per Ti site) between Ti-bonded and O_sH-bonded acetones on a TiO₂ surface (Scheme 2) with IPA spectators present; it is assumed that the adsorption of acetone and IPA at both Ti sites and O_sH groups, as well as the enolation step, are quasi-equilibrated (see section S10 in the SI for the detailed derivation):

$$r_{C-C} = \frac{k_{C-C}K_{Enolate}K_{one-Ti}K_{one-OH}P_{one}^2}{(1 + K_{one-Ti}P_{one} + K_{IPA-Ti}P_{IPA})(1 + K_{one-OH}P_{one} + K_{IPA-OH}P_{IPA})} \quad (2)$$

where P_{one} and P_{IPA} denote the partial pressures of acetone and IPA, respectively; K_{one-Ti} (or K_{IPA-Ti}) and K_{one-OH} (or K_{IPA-OH}) are the equilibrium constants for acetone (or IPA) adsorption on a Ti site and a O_sH group, respectively; $K_{Enolate}$ is the equilibrium constant for the enolation step (Step III, Scheme 2); r_{C-C} is the rate constant for the kinetically relevant C–C coupling step (Step IV, Scheme 2). We were unable to extract the value of the C–C coupling rate constant k_{C-C} using eq 2 and could only determine the combined term $k_{C-C}K_{Enolate}$. Under high P_{one} and low P_{IPA} and when both the Ti sites and O_sH groups are predominantly covered by acetone, eq 2 can be simplified and rewritten as

$$r_{C-C} = k_{C-C}K_{Enolate} \quad (3)$$

The direct kinetic measurement of an acetone-predominant surface, however, is unattainable because of the rapid deactivation of the catalyst (Figure 2). Therefore, Cu/SiO₂ cocatalysts and H₂ carrier gas were introduced in the kinetic measurement. On one hand, Cu/SiO₂ cocatalysts and H₂ helped mitigate the deactivation of the catalyst by hydrogenating the C=O and C=C bonds of the primary condensation products (mesityl oxide) and therefore suppressing the secondary condensation reactions,¹⁰ which allowed for reliable kinetic measurements under a low P_{IPA}/P_{one} ratio (e.g., 1/40) and high acetone coverage. On the other hand, with Cu/SiO₂ and H₂, we purposely adjusted the spectator-to-reactant ratio on the catalyst surface via IPA–acetone equilibrium in the gas phase:



We confirmed that adding Cu/SiO₂ cocatalysts and H₂ did not affect the kinetics of acetone condensation on TiO₂ by comparing the rates for acetone condensation (r_{C-C}) measured in the presence and absence of Cu/SiO₂ cocatalysts and H₂, respectively, under the same temperature and P_{IPA}/P_{one} ratio (Figure S12 in the SI).

Figure 7a and b shows r_{C-C} on TiO₂(101) and TiO₂(001) at 523 K as a function of P_{one} , and these four sets of kinetic data were acquired under constant P_{IPA}/P_{one} ratios of 1/40, 1/20, 1/10, and 1/5, respectively. The regression of these four sets of

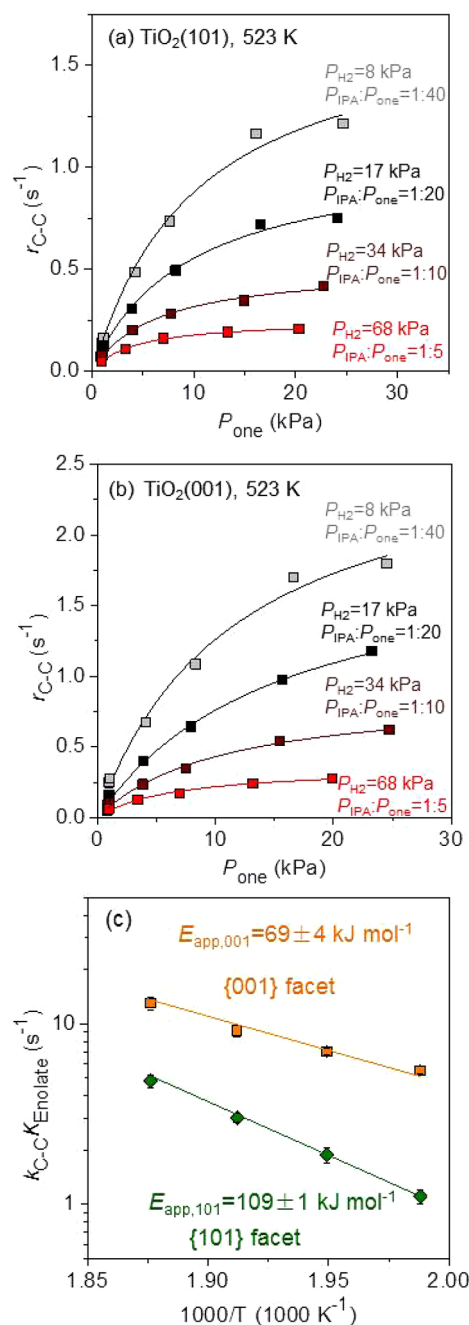


Figure 7. (a, b) Rates for acetone condensation (r_{C-C}) on TiO₂(101) + Cu/SiO₂(1:2 mass) and TiO₂(001) + Cu/SiO₂(1:1 mass) at 523 K as a function of acetone partial pressure (P_{one}) under the constant H₂ partial pressures of 8, 17, 34, and 68 kPa. (c) Arrhenius plots for the effective C–C coupling rate constant $k_{C-C}K_{Enolate}$ on the TiO₂ {101} and TiO₂ {001} facets.

kinetic data against eq 2 produced the value of the effective rate constant $k_{C-C}K_{Enolate}$ (see Figure S11 in the SI for the remaining data sets regarding TiO₂(101) and TiO₂(001) catalysts at different temperatures (503–533 K)).

Figure 7c shows the Arrhenius plots for the effective rate constants $k_{C-C}K_{Enolate}$ on TiO₂ {101} and {001} facets, respectively. The {001} facet has a higher rate constant $k_{C-C}K_{Enolate}$ and lower apparent activation energy ($E_{app} = 69 \pm 4$ and 109 ± 1 kJ mol⁻¹ for the {001} and {101} facets, respectively) than the {101} facet does. This activation energy trend is consistent with that estimated by DFT calculations

(121 vs 165 kJ mol⁻¹ for the TiO₂ {001} and {101} facets, respectively). This trend of acetone condensation activity is in line with the acetone TPD-DRIFTS results (Figure 5d), which show that acetone coverage decreases faster on a TiO₂{001} than on a TiO₂{101} catalyst. Next, we examined the properties of these two crystal facets to propose the possible reason for the lower activation barrier on the TiO₂ {001} facet.

As shown in Figure 6, the apparent activation energy for acetone condensation is a combination of the reaction energy for the quasi-equilibrated enolation step (Step III, Scheme 2) and the activation energy for the kinetically relevant C–C coupling step (Step IV, Scheme 2). DFT calculation results (Figure 6) show that although the enolation step is less favored on the {001} facet than on the {101} facet, the activation barrier for the intermolecular C–C coupling step is much lower on the {001} facet than on the {101} facet. This lower activation barrier results in a lower apparent activation energy for acetone condensation on the {001} facet.

It is postulated that the higher C–C coupling activity on the {001} facet is likely related to the earliness of the transition state (TS_{C–C}, Figure 6). The C–C coupling step is slightly exothermic on the {001} facet ($\Delta H = -2$ kJ mol⁻¹) but endothermic on the {101} facet ($\Delta H = 53$ kJ mol⁻¹). As a result, the {001} facet has an earlier TS_{C–C} compared to the {101} facet, as indicated by its longer C–C distance (3.04 Å on {001} vs 2.07 Å on {101}; Figure 6). This correlation between the earliness of the transition state and the exothermicity of the reaction is in line with Hammond's postulation.⁵⁵ As shown in Figure 6, the completion of the C–C coupling between the Ti_{5c}-bonded enolate and the O_sH-bonded acetone requires the proton transfer from O_sH to the aldol precursor and then partial desorption to form the adsorbed aldol (Figure 6). The O_sH-bonded acetone adsorbs more weakly on the {001} facet than on the {101} facet, as confirmed by both acetone TPD-DRIFTS (Figure 5d) and DFT calculations (adsorption energy -55 vs -87 kJ mol⁻¹), making the desorption easier on the {001} facet. On the other hand, the Brønsted base strength of the surface O_{2c} site is weaker on the {001} facet than on the {101} facet. Therefore, the reprotonation of the TS_{C–C} via proton transfer from the surface O_{2c} site to the aldol precursor is more favorable on the {001} facet. Together, these cause the C–C coupling step to require less energy and be more exothermic on the {001} facet. The {001} facet, which has a larger reaction exothermicity and an earlier transition state, has a lower activation barrier for this step according to the Brønsted–Evans–Polanyi principle.

Another possible reason for the higher C–C coupling activity on the {001} facet is related to the configuration of the catalyst surfaces because the intermolecular C–C coupling of two vicinal molecules could be sensitive to steric hindrance. Figure 6 presents the top and side views of the anatase TiO₂ {001} and {101} facets and shows that the {001} facet has a smoother surface geometric configuration compared to the {101} facet. The {001} facet is less hindered which likely favors C–C coupling between the Ti_{5c}-bonded enolate and the vicinal O_sH-bonded acetone. Also, the hindrance-free {001} surface better stabilizes the bimolecular TS_{C–C} and the aldol product, as indicated by the shorter CO–Ti_{5c} and COH–O_s bonding lengths of the TS_{C–C} and aldol product on the {001} facet (Figure 6), which lowers the activation energy of TS_{C–C}.

CONCLUSIONS

In this work, two types of anatase TiO₂ nanocrystals with preferential exposure of the {101} and {001} facets, respectively, were synthesized as model catalysts to probe the site requirements and elementary steps of acetone aldol condensation on Lewis acid–base site pairs. Temperature-dependent DRIFTS experiments showed the existence of abundant acetone bonded to surface hydroxyl groups (acetone–O_sH) and acetone bonded to Lewis acid sites (acetone–Ti_{5c}) on the surface of both {101} and {001} facet dominant TiO₂. Acetone condensation between an enolate formed on the Lewis acidic Ti_{5c} site and an acetone hydrogen-bonded to a vicinal surface O_sH group is the kinetically relevant step. The TiO₂ {001} facet has a lower apparent activation energy of acetone aldol condensation compared to the {101} facet, as confirmed by both DFT calculation and kinetic measurement experiments. Two possible reasons are proposed for the higher activity on the {001} facet: (1) The kinetically relevant C–C coupling step requires proton transfer from O_sH to the aldol precursor and then partial desorption to form the adsorbed aldol. The weaker Lewis acid and Brønsted base strengths of the {001} facet favors the proton transfer and desorption, making the C–C coupling step more exothermic on the {001} facets and resulting in an earlier transition state with a lower activation barrier. (2) The {001} facet has a smoother surface configuration than the {101} facet and less hindrance interfering with intermolecular C–C bond formation, meaning that TS_{C–C} is better stabilized on the {001} facet.

ASSOCIATED CONTENT

Supporting Information

The Supporting Information is available free of charge at <https://pubs.acs.org/doi/10.1021/jacsau.0c00028>.

Additional information about catalyst synthesis, titration of Lewis acid–base site pairs, estimation of the number of remaining Lewis acid sites during catalytic rate measurements, the kinetic isotope effect of acetone-*d*₆ on aldol condensation, DFT calculation results on dry and hydroxylated anatase TiO₂, DFT calculation of vibration frequencies of adsorbed acetone, DRIFTS spectra of in situ acetone-IPA adsorption on TiO₂, the impact of H₂ on acetone condensation activity on TiO₂, more detailed structures of DFT model and the overall energy diagram of acetone condensation on hydroxylated TiO₂, the derivation of a kinetic model for acetone condensation on a TiO₂ surface populated with OH groups and IPA spectators, and additional kinetic results for determining rate constants (PDF)

AUTHOR INFORMATION

Corresponding Authors

Huamin Wang – Institute for Integrated Catalysis, Pacific Northwest National Laboratory, Richland, Washington 99354, United States; orcid.org/0000-0002-3036-2649; Email: huamin.wang@pnnl.gov

Donghai Mei – Institute for Integrated Catalysis, Pacific Northwest National Laboratory, Richland, Washington 99354, United States; School of Chemistry and Chemical Engineering, Tiangong University, Tianjin 300387, China;

orcid.org/0000-0002-0286-4182; Email: dhmei@tiangong.edu.cn

Yong Wang – Institute for Integrated Catalysis, Pacific Northwest National Laboratory, Richland, Washington 99354, United States; The Gene and Linda Voiland School of Chemical Engineering and Bioengineering, Washington State University, Pullman, Washington 99164, United States; orcid.org/0000-0002-8460-7410; Email: yong.wang@pnnl.gov

Authors

Fan Lin – Institute for Integrated Catalysis, Pacific Northwest National Laboratory, Richland, Washington 99354, United States

Yuntao Zhao – Institute for Integrated Catalysis, Pacific Northwest National Laboratory, Richland, Washington 99354, United States

Jia Fu – School of Chemistry and Chemical Engineering, Tiangong University, Tianjin 300387, China

Nicholas R. Jaegers – Institute for Integrated Catalysis, Pacific Northwest National Laboratory, Richland, Washington 99354, United States; The Gene and Linda Voiland School of Chemical Engineering and Bioengineering, Washington State University, Pullman, Washington 99164, United States; orcid.org/0000-0002-9930-7672

Feng Gao – Institute for Integrated Catalysis, Pacific Northwest National Laboratory, Richland, Washington 99354, United States; orcid.org/0000-0002-8450-3419

Complete contact information is available at: <https://pubs.acs.org/10.1021/jacsau.0c00028>

Notes

The authors declare no competing financial interest.

ACKNOWLEDGMENTS

The authors acknowledge the U.S. Department of Energy (DOE), Office of Basic Energy Sciences, Division of Chemical Sciences, Geosciences, and Biosciences for funding this project (DE-AC05-RL01830). Part of this work was conducted in the William R. Wiley Environmental Molecular Sciences Laboratory (EMSL), a national scientific user facility sponsored by DOE's Office of Biological and Environmental Research and located at Pacific Northwest National Laboratory (PNNL). PNNL is a multiprogram national laboratory operated for the DOE by Battelle. Computing time was granted by a user proposal at EMSL and the National Energy Research Scientific Computing Center (NERSC).

REFERENCES

- (1) Huber, G. W.; Iborra, S.; Corma, A. Synthesis of Transportation Fuels from Biomass: Chemistry, Catalysts, and Engineering. *Chem. Rev.* **2006**, *106*, 4044–4098.
- (2) Alonso, D. M.; Bond, J. Q.; Dumesic, J. A. Catalytic conversion of biomass to biofuels. *Green Chem.* **2010**, *12*, 1493–1513.
- (3) Chheda, J. N.; Dumesic, J. A. An overview of dehydration, aldol-condensation and hydrogenation processes for production of liquid alkanes from biomass-derived carbohydrates. *Catal. Today* **2007**, *123*, 59–70.
- (4) Kozłowski, J. T.; Davis, R. J. Heterogeneous Catalysts for the Guerbet Coupling of Alcohols. *ACS Catal.* **2013**, *3*, 1588–1600.
- (5) Gabriëls, D.; Hernández, W. Y.; Sels, B.; Van Der Voort, P.; Verberckmoes, A. Review of catalytic systems and thermodynamics

for the Guerbet condensation reaction and challenges for biomass valorization. *Catal. Sci. Technol.* **2015**, *5*, 3876–3902.

(6) Chakraborty, S.; Pizzel, P. E.; Hayes, C. E.; Baker, R. T.; Jones, W. D. Highly Selective Formation of n-Butanol from Ethanol through the Guerbet Process: A Tandem Catalytic Approach. *J. Am. Chem. Soc.* **2015**, *137*, 14264–14267.

(7) Sun, J.; Wang, Y. Recent Advances in Catalytic Conversion of Ethanol to Chemicals. *ACS Catal.* **2014**, *4*, 1078–1090.

(8) Sun, J.; Zhu, K.; Gao, F.; Wang, C.; Liu, J.; Peden, C. H. F.; Wang, Y. Direct Conversion of Bio-ethanol to Isobutene on Nanosized Zn_xZr_yO_z Mixed Oxides with Balanced Acid–Base Sites. *J. Am. Chem. Soc.* **2011**, *133*, 11096–11099.

(9) Li, H.; Xu, Z.; Yan, P.; Zhang, Z. C. A catalytic aldol condensation system enables one pot conversion of biomass saccharides to biofuel intermediates. *Green Chem.* **2017**, *19*, 1751–1756.

(10) Wang, S.; Goulas, K.; Iglesia, E. Condensation and esterification reactions of alkanals, alkanones, and alkanols on TiO₂: Elementary steps, site requirements, and synergistic effects of bifunctional strategies. *J. Catal.* **2016**, *340*, 302–320.

(11) Zhang, H.; Ibrahim, M. Y. S.; Flaherty, D. W. Aldol condensation among acetaldehyde and ethanol reactants on TiO₂: Experimental evidence for the kinetically relevant nucleophilic attack of enolates. *J. Catal.* **2018**, *361*, 290–302.

(12) Young, Z. D.; Hanspal, S.; Davis, R. J. Aldol Condensation of Acetaldehyde over Titania, Hydroxyapatite, and Magnesia. *ACS Catal.* **2016**, *6*, 3193–3202.

(13) Raskó, J.; Kiss, J. Adsorption and surface reactions of acetaldehyde on TiO₂, CeO₂ and Al₂O₃. *Appl. Catal., A* **2005**, *287*, 252–260.

(14) Idriss, H.; Kim, K. S.; Barteau, M. A. Carbon-Carbon Bond Formation via Aldolization of Acetaldehyde on Single Crystal and Polycrystalline TiO₂ Surfaces. *J. Catal.* **1993**, *139*, 119–133.

(15) Luo, S.; Falconer, J. L. Acetone and Acetaldehyde Oligomerization on TiO₂ Surfaces. *J. Catal.* **1999**, *185*, 393–407.

(16) Zhao, L.; An, H.; Zhao, X.; Wang, Y. TiO₂-Catalyzed n-Valeraldehyde Self-Condensation Reaction Mechanism and Kinetics. *ACS Catal.* **2017**, *7*, 4451–4461.

(17) Wang, S.; Iglesia, E. Entropy-Driven High Reactivity of Formaldehyde in Nucleophilic Attack by Enolates on Oxide Surfaces. *J. Am. Chem. Soc.* **2018**, *140*, 775–782.

(18) Zaki, M. I.; Hasan, M. A.; Pasupulety, L. Surface Reactions of Acetone on Al₂O₃, TiO₂, ZrO₂, and CeO₂: IR Spectroscopic Assessment of Impacts of the Surface Acid-Base Properties. *Langmuir* **2001**, *17*, 768–774.

(19) Wang, S.; Iglesia, E. Substituent Effects and Molecular Descriptors of Reactivity in Condensation and Esterification Reactions of Oxygenates on Acid–Base Pairs at TiO₂ and ZrO₂ Surfaces. *J. Phys. Chem. C* **2016**, *120*, 21589–21616.

(20) Zhao, Y.; Zhu, X.; Wang, H.; Han, J.; Mei, D.; Ge, Q. Aqueous Phase Aldol Condensation of Formaldehyde and Acetone on Anatase TiO₂(101) Surface: A Theoretical Investigation. *ChemCatChem* **2020**, *12*, 1220–1229.

(21) Idriss, H.; Diagne, C.; Hindermann, J. P.; Kiennemann, A.; Barteau, M. A. Reactions of Acetaldehyde on CeO₂ and CeO₂-Supported Catalysts. *J. Catal.* **1995**, *155*, 219–237.

(22) Chen, S.; Yang, H.; Hu, C. Theoretical study on the reaction mechanisms of the aldol-condensation of 5-hydroxymethylfurfural with acetone catalyzed by MgO and MgO⁺. *Catal. Today* **2015**, *245*, 100–107.

(23) Díez, V. K.; Apesteguía, C. R.; Di Cosimo, J. I. Aldol condensation of citral with acetone on MgO and alkali-promoted MgO catalysts. *J. Catal.* **2006**, *240*, 235–244.

(24) Liang, D.; Li, G.; Liu, Y.; Wu, J.; Zhang, X. Controllable self-aldol condensation of cyclopentanone over MgO-ZrO₂ mixed oxides: Origin of activity & selectivity. *Catal. Commun.* **2016**, *81*, 33–36.

(25) Shen, W.; Tompsett, G. A.; Hammond, K. D.; Xing, R.; Dogan, F.; Grey, C. P.; Conner, W. C.; Auerbach, S. M.; Huber, G. W. Liquid

phase aldol condensation reactions with MgO-ZrO₂ and shape-selective nitrogen-substituted NaY. *Appl. Catal., A* **2011**, *392*, 57–68.

(26) Matsuda, S.; Kato, A. Titanium oxide based catalysts - a review. *Appl. Catal.* **1983**, *8*, 149–165.

(27) Chen, W.; Kuang, Q.; Wang, Q.; Xie, Z. Engineering a high energy surface of anatase TiO₂ crystals towards enhanced performance for energy conversion and environmental applications. *RSC Adv.* **2015**, *5*, 20396–20409.

(28) Hanna, D. G.; Shylesh, S.; Li, Y.-P.; Krishna, S.; Head-Gordon, M.; Bell, A. T. Experimental and Theoretical Study of n-Butanal Self-Condensation over Ti Species Supported on Silica. *ACS Catal.* **2014**, *4*, 2908–2916.

(29) Lin, F.; Chen, Y.; Zhang, L.; Mei, D.; Kovarik, L.; Sudduth, B.; Wang, H.; Gao, F.; Wang, Y. Single-Facet Dominant Anatase TiO₂(101) and (001) Model Catalysts to Elucidate the Active Sites for Alkanol Dehydration. *ACS Catal.* **2020**, *10*, 4268–4279.

(30) Hadjiivanov, K. I.; Klissurski, D. G. Surface chemistry of titania (anatase) and titania-supported catalysts. *Chem. Soc. Rev.* **1996**, *25*, 61–69.

(31) Lin, H.; Long, J.; Gu, Q.; Zhang, W.; Ruan, R.; Li, Z.; Wang, X. In situ IR study of surface hydroxyl species of dehydrated TiO₂: towards understanding pivotal surface processes of TiO₂ photocatalytic oxidation of toluene. *Phys. Chem. Chem. Phys.* **2012**, *14*, 9468–9474.

(32) Perdew, J. P.; Burke, K.; Ernzerhof, M. Generalized Gradient Approximation Made Simple. *Phys. Rev. Lett.* **1996**, *77*, 3865.

(33) VandeVondele, J.; Krack, M.; Mohamed, F.; Parrinello, M.; Chassaing, T.; Hutter, J. Quickstep: Fast and Accurate Density Functional Calculations Using a Mixed Gaussian and Plane Waves Approach. *Comput. Phys. Commun.* **2005**, *167*, 103–128.

(34) Goedecker, S.; Teter, M.; Hutter, J. Separable Dual-Space Gaussian Pseudopotentials. *Phys. Rev. B: Condens. Matter Mater. Phys.* **1996**, *54*, 1703–1710.

(35) Hartwigsen, C.; Goedecker, S.; Hutter, J. Relativistic Separable Dual-Space Gaussian Pseudopotentials from H to Rn. *Phys. Rev. B: Condens. Matter Mater. Phys.* **1998**, *58*, 3641–3662.

(36) Krack, M.; Parrinello, M. All-electron *ab-initio* Molecular Dynamics. *Phys. Chem. Chem. Phys.* **2000**, *2*, 2105–2112.

(37) Grimme, S.; Antony, J.; Ehrlich, S.; Krieg, H. A Consistent and Accurate *ab initio* Parametrization of Density Functional Dispersion Correction (DFT-D) for the 94 Elements H-Pu. *J. Chem. Phys.* **2010**, *132*, 154104.

(38) De Angelis, F.; Di Valentin, C.; Fantacci, S.; Vittadini, A.; Selloni, A. Theoretical Studies on Anatase and Less Common TiO₂ Phases: Bulk, Surfaces, and Nanomaterials. *Chem. Rev.* **2014**, *114*, 9708–9753.

(39) Selcuk, S.; Selloni, A. Facet-dependent trapping and dynamics of excess electrons at anatase TiO₂ surfaces and aqueous interfaces. *Nat. Mater.* **2016**, *15*, 1107–1112.

(40) Capdevila-Cortada, M.; Łodziana, Z.; López, N. Performance of DFT+U Approaches in the Study of Catalytic Materials. *ACS Catal.* **2016**, *6*, 8370–8379.

(41) Deskins, N. A.; Dupuis, M. Electron transport via polaron hopping in bulk TiO₂: A density functional theory characterization. *Phys. Rev. B: Condens. Matter Mater. Phys.* **2007**, *75*, 195212.

(42) Mattsson, A.; Leideborg, M.; Larsson, K.; Westin, G.; Österlund, L. Adsorption and Solar Light Decomposition of Acetone on Anatase TiO₂ and Niobium Doped TiO₂ Thin Films. *J. Phys. Chem. B* **2006**, *110*, 1210–1220.

(43) Singh, M.; Zhou, N.; Paul, D. K.; Klabunde, K. J. IR spectral evidence of aldol condensation: Acetaldehyde adsorption over TiO₂ surface. *J. Catal.* **2008**, *260*, 371–379.

(44) Busca, G.; Lamotte, J.; Lavalley, J. C.; Lorenzelli, V. FT-IR study of the adsorption and transformation of formaldehyde on oxide surfaces. *J. Am. Chem. Soc.* **1987**, *109*, 5197–5202.

(45) Panov, A.; Fripiat, J. J. An Infrared Spectroscopic Study of Acetone and Mesityl Oxide Adsorption on Acid Catalyst. *Langmuir* **1998**, *14*, 3788–3796.

(46) Okunev, A. G.; Paukshtis, E. A.; Aristov, Y. I. Acetone adsorption on hydroxylated silica gel: Correlation of sorption isotherms and IR spectra. *React. Kinet. Catal. Lett.* **1998**, *65*, 161–167.

(47) NIST Chemistry WebBook: NIST Standard Reference Database Number 69.

(48) Herman, G. S.; Sievers, M. R.; Gao, Y. Structure Determination of the Two-Domain (1 × 4) Anatase TiO₂(001) Surface. *Phys. Rev. Lett.* **2000**, *84*, 3354–3357.

(49) Liang, Y.; Gan, S.; Chambers, S. A.; Altman, E. I. Surface structure of anatase TiO₂(001): Reconstruction, atomic steps, and domains. *Phys. Rev. B: Condens. Matter Mater. Phys.* **2001**, *63*, 235402.

(50) Wang, Y.; Sun, H.; Tan, S.; Feng, H.; Cheng, Z.; Zhao, J.; Zhao, A.; Wang, B.; Luo, Y.; Yang, J.; Hou, J. G. Role of point defects on the reactivity of reconstructed anatase titanium dioxide (001) surface. *Nat. Commun.* **2013**, *4*, 2214.

(51) Yuan, W.; Zhu, B.; Li, X.-Y.; Hansen, T. W.; Ou, Y.; Fang, K.; Yang, H.; Zhang, Z.; Wagner, J. B.; Gao, Y.; Wang, Y. Visualizing H₂O molecules reacting at TiO₂ active sites with transmission electron microscopy. *Science* **2020**, *367*, 428–430.

(52) Yuan, W.; Wang, Y.; Li, H.; Wu, H.; Zhang, Z.; Selloni, A.; Sun, C. Real-Time Observation of Reconstruction Dynamics on TiO₂(001) Surface under Oxygen via an Environmental Transmission Electron Microscope. *Nano Lett.* **2016**, *16*, 132–137.

(53) Hengerer, R.; Bolliger, B.; Erbudak, M.; Grätzel, M. Structure and stability of the anatase TiO₂(101) and (001) surfaces. *Surf. Sci.* **2000**, *460*, 162–169.

(54) Ngo, D. T.; Tan, Q.; Wang, B.; Resasco, D. E. Aldol Condensation of Cyclopentanone on Hydrophobized MgO. Promotional Role of Water and Changes in the Rate-Limiting Step upon Organosilane Functionalization. *ACS Catal.* **2019**, *9*, 2831–2841.

(55) Hammond, G. S. A Correlation of Reaction Rates. *J. Am. Chem. Soc.* **1955**, *77*, 334–338.